



A First Look at the Abundance Pattern—O/H, C/O, and Ne/O—in $z > 7$ Galaxies with JWST/NIRSpec

Karla Z. Arellano-Córdova¹ , Danielle A. Berg¹ , John Chisholm¹ , Pablo Arrabal Haro² , Mark Dickinson² , Steven L. Finkelstein¹ , Floriane Leclercq¹ , Noah S. J. Rogers³ , Raymond C. Simons⁴ , Evan D. Skillman³ , Jonathan R. Trump⁵ , and Jeyhan S. Kartaltepe⁶

¹ Department of Astronomy, The University of Texas at Austin, 2515 Speedway, Stop C1400, Austin, TX 78712, USA; kzarellano@austin.utexas.edu

² NSF's National Optical-Infrared Astronomy Research Laboratory, 950 North Cherry Avenue, Tucson, AZ 85719, USA

³ Minnesota Institute for Astrophysics, University of Minnesota, 116 Church Street SE, Minneapolis, MN 55455, USA

⁴ Space Telescope Science Institute, 3700 San Martin Drive, Baltimore, MD, 21218, USA

⁵ Department of Physics, 196 Auditorium Road, Unit 3046, University of Connecticut, Storrs, CT 06269, USA

⁶ Laboratory for Multiwavelength Astrophysics, School of Physics and Astronomy, Rochester Institute of Technology, 84 Lomb Memorial Drive, Rochester, NY 14623, USA

Received 2022 August 4; revised 2022 October 7; accepted 2022 October 10; published 2022 November 21

Abstract

We analyze the rest-frame near-UV and optical nebular spectra of three $z > 7$ galaxies from the Early Release Observations taken with the Near-Infrared Spectrograph (NIRSpec) on the James Webb Space Telescope (JWST). These three high- z galaxies show the detection of several strong emission nebular lines, including the temperature-sensitive [O III] $\lambda 4363$ line, allowing us to directly determine the nebular conditions and abundances for O/H, C/O, and Ne/O. We derive O/H abundances and ionization parameters that are generally consistent with other recent analyses. We analyze the mass–metallicity relationship (i.e., slope) and its redshift evolution by comparing between the three $z > 7$ galaxies and local star-forming galaxies. We also detect the C III] $\lambda \lambda 1907, 1909$ emission in a $z > 8$ galaxy from which we determine the most distant C/O abundance to date. This valuable detection of $\log(C/O) = -0.83 \pm 0.38$ provides the first test of C/O redshift evolution out to high redshift. For neon, we use the high-ionization [Ne III] $\lambda 3869$ line to measure the first Ne/O abundances at $z > 7$, finding no evolution in this α -element ratio. We explore the tentative detection of [Fe II] and [Fe III] lines in a $z > 8$ galaxy, which would indicate a rapid buildup of metals. Importantly, we demonstrate that properly flux-calibrated and higher-S/N spectra are crucial to robustly determine the abundance pattern in $z > 7$ galaxies with NIRSpec/JWST.

Unified Astronomy Thesaurus concepts: [Galaxy chemical evolution \(580\)](#); [Emission line galaxies \(459\)](#); [Cosmic abundances \(315\)](#); [Metallicity \(1031\)](#)

1. Introduction

Theory predicts that the first galaxies were composed nearly entirely of hydrogen and helium with trace amounts of heavier metals. As massive stars synthesized metals in their cores and injected these metals into the interstellar medium (ISM), galaxies quickly built up their metal content over time (Tinsley 1980). This chemical enrichment of galaxies has been observed at moderate and low redshifts with the establishment and evolution of the mass–metallicity relation (MZR; e.g., Tremonti et al. 2004; Dalcanton 2007; Peeples & Shankar 2011; Zahid et al. 2014). However, the compositions of the first galaxies, and the ancestors of local galaxies, have remained beyond characterization due to the faint nature and redshifted emission lines. The ISM of such early universe galaxies, where little chemical evolution has occurred, provides benchmarks for our understanding of how galaxies form and evolve via their chemical enrichment pathways.

Additionally, there is a general consensus that metal-poor, low-mass galaxies hosted a large fraction of the star formation in the high-redshift universe and were, therefore, the dominant contributors to reionizing the early universe (e.g., Wise et al. 2014; Madau & Haardt 2015). Determining the precise epoch

and source of reionization is currently a major focus of observational cosmology, yet the relative ionizing radiation contributions from stellar versus accretion activity are still uncertain (e.g., Fontanot et al. 2014). Depending on the model assumptions (i.e., redshift, luminosity function, intergalactic medium [IGM] clumping factor, and ionizing photon production efficiency), the estimated escape fraction of ionizing radiation needed to sustain cosmic reionization ranges from $< 5\%$ (Finkelstein et al. 2019) up to 21% (Naidu et al. 2020). On the other hand, recent observations have emphasized the role of dust in regulating the escape of ionizing photons based on the direct empirical relation between the observed Lyman continuum (LyC) escape fraction and the slope of the far-ultraviolet (FUV) stellar continuum (e.g., Chisholm et al. 2022; Saldana-Lopez et al. 2022). Given the strong trend between dust content and metallicity (e.g., Li et al. 2019; Shapley et al. 2020), accurate abundance determinations are crucial to understanding the escape of ionizing photons from galaxies within the epoch of reionization. Further, recent $z \sim 3$ observations highlight the impact of evolving abundance ratios on the production and hardness of ionizing photons (Steidel et al. 2016). The first galaxies shaped the conditions within the IGM and set the initial conditions for all subsequent galaxy evolution. A detailed study of chemically unevolved galaxies at early epochs is required to establish the physical conditions that produced the ionizing photons to reionize the early universe.

Very few high-redshift galaxies ($z > 3$) have been observed in spectroscopic detail owing to the challenges of observing their rest-frame optical spectra through the ground-based transparency windows of the infrared. Fortunately, the successful launch of the James Webb Space Telescope (JWST) has opened a new window on high-redshift galaxy spectroscopy, pushing the FUV and optical spectroscopic frontiers to higher redshifts than ever before. However, the success of such observations hinges on our ability to interpret the gaseous conditions, especially the abundance pattern, that power the observed spectral features.

Here we examine the Early Release Observations (EROs) of the Near-Infrared Spectrograph (NIRSpec; Jakobsen et al. 2022) on JWST of the three $z > 7$ galaxies in the SMACS J0723.3–732 cluster field and interpret their nebular properties. We specifically focus on our ability to determine robust nebular properties, such as the electron temperature and ionization parameter, and the O/H, C/O, Ne/O, and Fe/O abundance composition. While O/H is the standard measure of a galaxy’s metallicity, the relative abundances of non- α elements (e.g., C, N, and Fe) have been observed to significantly deviate from solar, especially in the metal-poor environments (e.g., Berg et al. 2019b, 2021).

Relative C and Fe abundances are especially important, as they are significant contributors to interstellar dust (e.g., Draine 2011), tracers of the physical conditions in nebular gas, and important sources of opacity in stars, affecting the time evolution of stellar winds and isochrones. Additionally, enhanced α /Fe (α /C) abundance ratios could produce harder radiation fields than expected from the O/H abundances in moderate-metallicity (low-metallicity; $Z_{\text{neb}} < 0.1 Z_{\odot}$) galaxies (e.g., Steidel et al. 2018; Shapley et al. 2019; Topping et al. 2020). Additionally, C is observable in high-redshift galaxies both in the rest-frame ultraviolet via C III] λ 1907, [C III] λ 1909 (e.g., Stark 2016; Hutchison et al. 2019) and in the rest-frame far-infrared via C II 158 μ m (e.g., Lagache et al. 2018), providing two paths to estimate the C abundance. Because C is primarily produced in lower-mass stars than O, the injection of C and O into the ISM occurs on different timescales, providing a probe of the duration, history, and burstiness of the star formation (e.g., Henry et al. 2000; Berg et al. 2019b).

The remainder of this paper is structured as follows. In Section 2, we describe the NIRSpec observations and data analysis. Section 3 describes the measurements of the redshift and the nebular emission lines. In Section 4, we discuss the calculations of nebular abundances, focusing on the oxygen abundance, the C/O abundance ratio, and the Fe/O flux ratio. Section 5 explores the O/H, C/O, and Ne/O evolution of galaxies from $z \sim 0$ to 8.5. Our final remarks are summarized in Section 6. Throughout this paper, we adopt a flat FRW metric with $\Omega_m = 0.3$, $\Omega_\Lambda = 0.7$, and $H_0 = 70 \text{ km s}^{-1} \text{ Mpc}^{-1}$ and the solar metallicity scale of Asplund et al. (2021), where $12 + \log(\text{O}/\text{H})_{\odot} = 8.69$, $\log(\text{C}/\text{O})_{\odot} = -0.23$, $\log(\text{Ne}/\text{O})_{\odot} = -0.63$, and $\log(\text{Fe}/\text{O})_{\odot} = -1.23$.

2. Sample Properties and Observations

We consider here the three lensed galaxies of the SMACS J0723.3–7327 galaxy cluster at $z > 7$, which have the JWST source IDs s04590, s06355, and s10612. The object ID numbers come from the input source catalog used for the NIRSpec microshutter array (MSA; Ferruit et al. 2022) configuration planning. These objects are gravitationally lensed

galaxies by a massive galaxy cluster at $z = 0.3877$, discovered by the southern extension of the Massive Cluster Survey (MACS; Ebeling et al. 2001; Repp & Ebeling 2018).

This cluster was observed with NIRSpec of JWST as a part of the EROs released on 2022 July 12 (program ID: 2736; Pontoppidan et al. 2022). NIRSpec medium-resolution gratings cover a wavelength range of 0.6–5.2 μ m at spectral resolution $R = \lambda/\Delta\lambda = 1000$ (Jakobsen et al. 2022). For these observations, each 1D spectrum was produced from the combination of two gratings/filters, G235M/F170LP (1.75–3.15 μ m) and G395M/F290LP (2.9–5.2 μ m), with a total exposure time of 8754 s in each of the two visits.

For the computation and analysis of the physical properties and chemical abundances of these high- z galaxies, we use the postprocessed NIRSpec spectra presented in Trump et al. (2022), which uses the pipeline of P. Arrabal Haro et al. in preparation, and compare it to the original JWST Science Calibration Pipeline v1.6.1⁷ data. In order to avoid emission from other sources or detector artifacts, the 1D postprocessed spectra were extracted using a narrow custom aperture centered at the location of the emission peaks within each slit. The postprocessing flux calibration was derived from the response of flat-spectrum pointlike sources in the Cosmic Evolution Early Release Science (CEERS; PI: S. Finkelstein; Finkelstein et al. 2022) simulations performed making use of the NIRSpec Instrument Performance Simulator (Piqueras et al. 2010). The details of these new postprocessed data will be presented in P. Arrabal Haro et al. 2022, in preparation.

The resulting postprocessed spectra of s04590, s06355, and s10612 are shown in Figure 1. The two visits of both s06355 and s10612, o007 and o008, are very similar in both flux and noise levels. However, even after the postprocessing, we find the same emission line flux measurement offsets for the two visits of s04590 as Trump et al. (2022). As a result, Trump et al. (2022) recommend only using emission line ratios of nearby lines. Further, Curti et al. (2023) recently inspected the 2D NIRSpec spectra and revealed an issue with the spectrum of the o007 visit of s04590 because the shutter [3, 27, 167] did not open. Therefore, we separate and call out calculations of the metallicity and other physical parameters of s04590 made with the o007 observation for this reason. However, we use the o007 observations only for comparison reasons in Section 4.1. This allows us to have consistent estimates of the physical properties of the gas despite the caveats due to absolute flux calibration of the data (see discussion in Trump et al. 2022).

3. Measurements

The JWST/NIRSpec spectra detect several rest-frame optical nebular emission lines in the two different visits (o007 and o008) for s04590, s06355, and s10612, which provide the opportunity to measure the redshift and important physical properties, including the reddening, total and relative metallicities, and ionization parameter.

3.1. Source Redshift

We have measured the systemic redshift of s04590, s06355, and s10612 using the most reliable strong emission lines in the spectra covered by NIRSpec. Specifically, we measured the observed central wavelengths of the five strongest emission

⁷ <https://jwst-pipeline.readthedocs.io/en/latest/jwst/introduction.html>

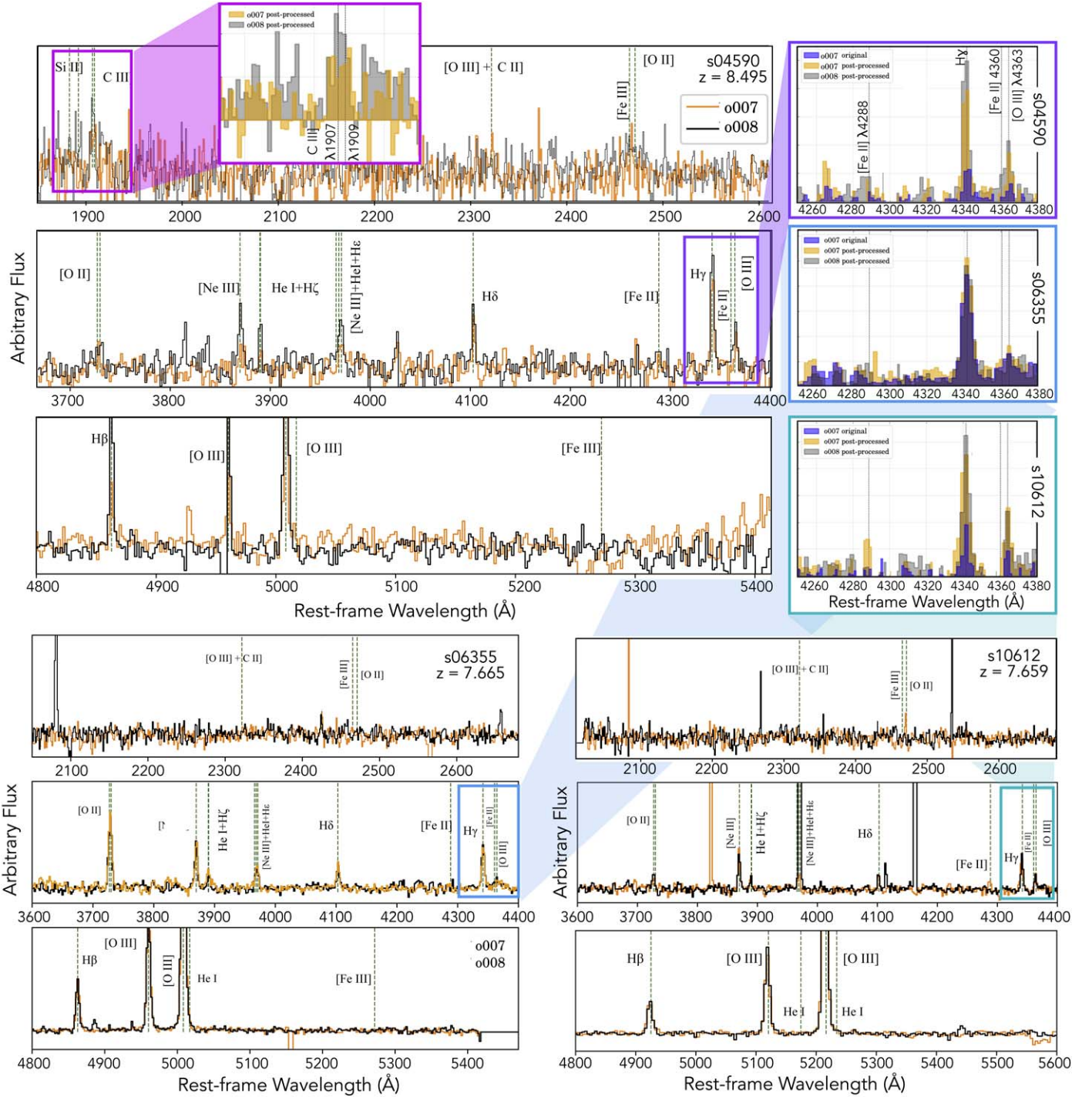


Figure 1. The JWST/NIRSpec postprocessed rest-frame spectra of s04590, s06355, and s10612. Wavelength ranges highlighting the important nebular emission line detections are shown. The orange and black spectra correspond to the o007 and o008 visits, respectively, for each galaxy. We highlight the detection of essential emission lines, such as C III] $\lambda\lambda 1906, 1906$, [Ne III] $\lambda 3869$, H γ $\lambda 4101$, H δ $\lambda 4340$, [O III] $\lambda 4363$, H β $\lambda 4861$, and [O III] $\lambda 5007$, and the tentative detection of [Fe III] $\lambda 2465$ in s04590. The inset spectra to the right highlight the differences between the original JWST Science Calibration Pipeline spectrum and the postprocessed spectrum (Trump et al. 2022; P. Arrabal Haro et al., in preparation) for the H γ and [O III] $\lambda 4363$ spectral features. The orange and black spectra correspond to the two different postprocessed spectra for the same galaxy, labeled as o007 and o008, respectively, and the original o007 reduction is shown in blue. For all three galaxies, the postprocessed spectra show a higher S/N in the emission lines.

lines in the NIRSpec spectrum (H δ , H γ , H β , and [O III] $\lambda\lambda 4959, 5007$) using Gaussian profile fits. Relative to the rest-frame vacuum wavelengths, we determine average redshifts of 8.495 for s04590, 7.665 for s06355, and 7.659 for s10612. Our estimated redshifts are in agreement with those published recently by Brinchmann (2022) Carnall et al. (2023), Schaerer et al. (2022), and Trump et al. (2022).

3.2. Nebular Emission Lines

Nebular emission lines are an important source of information, providing the chemical composition and physical properties of the ionized gas (e.g., Kewley et al. 2019; Maiolino & Mannucci 2019). In this context, significant rest-frame UV and optical emission line detections are essential to analyzing the

physical properties of galaxies across cosmic time. Therefore, the accurate emission line ratios are vital to determining extragalactic metallicities and, subsequently, constraining fundamental galaxy trends, such as the MZR across cosmic time.

To ensure accurate measurements of the emission lines in the NIRSpect observations, we use IRAF⁸ to carefully inspect and measure the fluxes of each individual nebular emission feature in each of the two visits available per galaxy. Specifically, we measured the fluxes by first determining the local continuum on each side of an isolated emission line and then integrating above the continuum. For those lines that appear blended, we fit multicomponent Gaussian profiles. The errors in the flux were calculated using the expression reported in Berg et al. (2013) and Rogers et al. (2021), which accounts for uncertainties in the flux calibration and sky subtraction. For the NIRSpect spectra, the dominant uncertainty comes from the flux calibration. Similar to Trump et al. (2022), we find a factor of 2 difference between the absolute fluxes of the o007 and o008 visits of s04590, while the two visits of s06355 and s10612 match very well. To account for the potentially very large uncertainty in absolute flux calibration, we increased the flux calibration uncertainty to 20% and (following the recommendation of Trump et al. 2022) used nearby line ratios when possible. In Table 1, we report the observed and corrected intensities with respect to $H\beta$ for the three high- z galaxies. Such optical emission lines are detected with a signal-to-noise (S/N) or $F_\lambda/\delta F_\lambda$ larger than 3. The UV lines reported in Table 1 for s04590 show detection with an $S/N < 3$ (i.e., C III] $\lambda 1907$, 1909).

3.3. Reddening

The large uncertainty associated with the flux calibration provides a particular challenge for determining the reddening due to dust from the Balmer decrement, which spans a large wavelength range. We therefore determine a primitive estimate of the reddening due to dust using the differences between the observed and theoretical values of the Balmer decrement and by assuming Case B recombination and typical nebular conditions (i.e., $T_e = 18,000$ K and $n_e = 100$ cm⁻³) corresponding to theoretical values of $H\gamma/H\beta = 0.47$ and $H\delta/H\beta = 0.26$ (calculated using the PyNeb package; Luridiana et al. 2015).

For all three galaxies, the $H\gamma/H\beta$ ratios are larger than physical but consistent between the two different visits (o007 and o008) in each galaxy. The observed values of $H\gamma/H\beta$ range between 0.40 and 0.50, which implies $E(B - V)$ values between -0.09 and -0.32 . In particular, the spectrum of the o007 visit of s04590 provide an observed value of $H\gamma/H\beta \sim 1$ (see also discussion in Trump et al. 2022). We therefore calculate the color excess, $E(B - V)$, based on only $H\delta/H\beta$ (0.20–0.22). Note that we used the $E(B - V)$ value derived from the o008 visit of s04590 to correct the o007 spectrum. Emission line fluxes were then corrected for reddening using the Cardelli et al. (1989) reddening law for the rest-frame optical lines and the Reddy et al. (2016) reddening law for the rest-frame UV lines.

The resulting $E(B - V)$ values are reported in Table 2, with values range between 0.31 and 0.34. Such $E(B - V)$ values are typical of $z \sim 0$ galaxies but perhaps surprising for such chemically young high- z galaxies. Given the significant flux calibration uncertainty, we adopt these $E(B - V)$ values as upper limits and explore their effect by determining abundances assuming both the $E(B - V)$ upper limits and a $E(B - V)$ lower limit of zero in Section 4.2.1.

4. Electron Temperature and Metallicity Determinations

The gas-phase metallicity of a galaxy is a key piece in the puzzle to understanding its evolution. Accurate abundance determinations require knowing the physical gas conditions. While nebular abundances are insensitive to the typical range of observed electron densities ($10^1 < n_e(\text{cm}^{-3}) < 10^3$), nebular emission lines are exponentially dependent on the electron temperature. For high-ionization galaxies, such as the $z > 7$ NIRSpect galaxies investigated here (see Section 4.2.2), a measure of the high-ionization temperature via the [O III] $\lambda 4363/\lambda 5007$ ratio is needed. Here we investigate the intrinsically faint, temperature-sensitive [O III] $\lambda 4363$ auroral line in s04950, s06355, and s01612. The detection of this line suggests that detailed cosmic abundance determinations will be possible with JWST for more distant galaxies than ever before. Below, we use the PyNeb package (version 1.1.14; Luridiana et al. 2015) in Python to calculate the physical conditions and chemical abundances in s04950, s06355, and s10612. We follow the same procedure and atomic data described in Berg et al. (2021) and Arellano-Córdova et al. (2022). For Ne and C, we have used the atomic data reported in Arellano-Córdova et al. (2020) and Berg et al. (2019b), respectively.

4.1. The T_e -sensitive [O III] $\lambda 4363$ Line

A number of low- and high-ionization emission lines are evident in the JWST/NIRSpect spectra of s04950, s06355, and s01612. Given the high redshift of these galaxies, the detection of weak, high-ionization emission lines such as [O III] $\lambda 4363$ that allow the computation of the electron temperature of the nebular gas (see Figure 1) is spectacular. We used the [O III] $\lambda 4363/\lambda 5007$ line ratio from the postprocessed spectra presented in Trump et al. (2022) to calculate the electron temperature in the $z > 7$ galaxies. For visit o008 of s04590, we calculate a very high electron temperature that is near the H-cooling limit of 2.41×10^4 K, while for the o007 visit, we assume $T_e = 16,000$ K (which is a representative value of local star-forming galaxies) due to the nonphysical value of $T_e([\text{O III}])$ determined using the [O III] $\lambda 4363/\lambda 5007$ line ratio (see also Schaerer et al. 2022). For s06355 and s10612, we calculate $T_e([\text{O III}])$ values for both the o007 and o008 spectra, finding $\Delta T_e = 1.5 \times 10^3$ K for s06355 and $\Delta T_e = 4.8 \times 10^3$ K for s10612. The calculated electron temperatures are reported in Table 2.

To investigate the large differences in the calculated electron temperatures, we compare the $H\gamma + [\text{O III}] \lambda 4363$ spectral range in the o007 and o008 visits of each galaxy in the inset panels of Figure 1. The narrow aperture extraction 1D spectrum used in this analysis (Trump et al. 2022; P. Arrabal Haro et al. 2022, in preparation; gray and orange spectra) has a higher S/N than the o007 original JWST Science Calibration Pipeline data (blue spectra). All three spectra display a clear detection of $H\gamma$ and [O III] $\lambda 4363$ for the narrow aperture extraction

⁸ IRAF is distributed by the National Optical Astronomy Observatory, which is operated by the Association of Universities for Research in Astronomy, Inc., under cooperative agreement with the National Science Foundation.

Table 1
Observed and Corrected Line Intensities with Respect to $H\beta = 100$ for s04590, s06355, and s10612

s04590						
λ_0	Ion	o007 ^a		o008		
		$F(\lambda)$	$I(\lambda)$	$F(\lambda)$	$I(\lambda)$	
1909 ^b	[C III]	53.1 ± 22.2	212.56 ± 95	21.6 ± 7.8	86.4 ± 34.0	
2465	[Fe III]	6.6 ± 2.7	18.1 ± 7.8	
3727	[O II]	21.9 ± 0.6	30.9 ± 1.51	15.9 ± 0.5	22.5 ± 1.1	
3869	[Ne III]	14.6 ± 0.4	19.9 ± 0.91	26.7 ± 0.8	36.5 ± 1.7	
4101	H δ	46.1 ± 1.3	58.9 ± 2.35	20.7 ± 0.6	26.4 ± 1.1	
4341	H γ	99.9 ± 2.8	118.3 ± 4.05	42.0 ± 1.2	49.7 ± 1.7	
4360 ^c	[Fe II]	3.37 ± 0.10	3.97 ± 0.13	
4363	[O III]	33.9 ± 1.0	39.8 ± 1.34	12.1 ± 1.7	14.2 ± 2.0	
4959	[O III]	106.5 ± 3.0	103.6 ± 2.95	
5007	[O III]	366.1 ± 10.4	351.6 ± 10.08	330.2 ± 9.3	317.1 ± 9.1	
$F(H\beta)$		1.18 ± 0.02		3.37 ± 0.06		

s06355						
λ_0	Ion	o007		o008		
		$F(\lambda)$	$I(\lambda)$	$F(\lambda)$	$I(\lambda)$	
3727	[O II]	76.4 ± 2.2	111.1 ± 5.3	80.0 ± 2.3	105.1 ± 5.3	
3869	[Ne III]	39.0 ± 1.1	54.6 ± 2.5	42.0 ± 1.2	53.7 ± 2.5	
4101	H δ	20.3 ± 0.6	26.5 ± 1.1	21.7 ± 0.6	26.4 ± 1.1	
4341	H γ	40.2 ± 1.1	48.2 ± 1.6	43.6 ± 1.2	49.8 ± 1.7	
4363	[O III]	11.6 ± 0.3	13.8 ± 2.0	9.6 ± 1.7	10.9 ± 2.0	
4959	[O III]	245.2 ± 6.9	238.0 ± 6.8	257.0 ± 7.3	251.4 ± 7.2	
5007	[O III]	822.9 ± 23.3	787.7 ± 22.6	834.3 ± 23.6	808.1 ± 23.2	
$F(H\beta)$		2.24 ± 0.04		2.27 ± 0.05		

s10612						
λ_0	Ion	o007		o008		
		$F(\lambda)$	$I(\lambda)$	$F(\lambda)$	$I(\lambda)$	
3727	[O II]	14.8 ± 0.4	20.83 ± 1.0	32.4 ± 0.9	41.1 ± 2.0	
3869	[Ne III]	45.8 ± 1.3	62.38 ± 2.8	52.9 ± 1.5	65.7 ± 3.0	
4101	H δ	20.7 ± 0.6	26.4 ± 1.0	22.3 ± 0.6	26.4 ± 1.0	
4341	H γ	49.8 ± 1.4	58.8 ± 2.0	48.6 ± 1.4	54.6 ± 1.9	
4363	[O III]	22.4 ± 0.6	26.21 ± 2.0	18.1 ± 1.8	20.2 ± 2.0	
4959	[O III]	209.2 ± 5.9	203.61 ± 5.8	248.6 ± 7.0	243.9 ± 6.9	
5007	[O III]	666.5 ± 18.9	640.44 ± 18.4	730.0 ± 20.6	709.9 ± 20.3	
$F(H\beta)$		1.37 ± 0.03		1.28 ± 0.03		

Notes.

^a The o007 spectrum of s04590 is affected by shutter closures (see Curti et al. 2023).

^b C III] λ 1907 + [C III] λ 1909.

^c The excess blue profile in [O III] λ 4363 is associated with the possible detection of [Fe II] λ 4360 in s04590 (see Figure 1). The observed $H\beta$ fluxes in units of 10^{-16} erg s $^{-1}$ cm $^{-2}$ \AA^{-1} .

postprocessed 1D spectra. Focusing on the postprocessed spectra, there are noticeable differences between the o007 and o008 spectra of s04590. While the profile shapes are consistent between the o007 and o008 visits of s06355 and s10612, the [O III] λ 4363 profile shapes of s04590 differ. Specifically, the o008 visit of s04590 shows excess flux blueward of the [O III] λ 4363 line center.

The source of the excess blue [O III] λ 4363 flux in the s04590 o008 visit is uncertain. The [Fe II] λ 4360 emission may be strong enough to contaminate [O III] λ 4360 at moderate metallicities (e.g., Curti et al. 2017; Arellano-Córdova & Rodríguez 2020; Berg et al. 2020; Rogers et al. 2021, 2022). However, these authors have only observed significant [Fe II] λ 4360 in high-metallicity $z = 0$ environments ($12 + \log(O/H) \sim 8.4$). How this applies to high- z environments is still unclear. In the case of s04590, the center of the excess blue flux aligns extremely well with the vacuum wavelength of the [Fe II]

λ 4360 line. Fitting for the potential [Fe II] λ 4360 line simultaneously with the [O III] λ 4363 line results in a 3σ [Fe II] detection that is 22% of the strength of the blended line flux. If not corrected for, [Fe II] contamination could lead to an overestimate of the $T_e([O III])$.

Unfortunately, other evidence for significant Fe emission is weak or uncertain. In the case of detectable [Fe II] λ 4360 emission, [Fe II] λ 4288 emission, which arises from the same orbital level as [Fe II] λ 4360 (see details in Méndez-Delgado et al. 2021), is expected at higher flux. As shown in the Figure 1 inset windows, weak [Fe II] λ 4288 maybe present, but only at the 1σ level in the current s04590 visits. On the other hand, the detection of the excess blue flux in [O III] λ 4363 is only visible in the o008 spectrum, which might indicate the presence of a possible artifact affecting the flux and profile of [O III] λ 4363. This emphasizes that the current JWST observations present significant instrumental artifacts that must be

Table 2
Derived Galaxy Properties, Metallicities, and Ionization Parameter

Property	s04590			s06335			s10612		
	<i>o007</i> ^a	o008	Δ	o007	o008	Δ	o007	o008	Δ
z	8.495		8.495	7.665	7.665		7.659	7.659	
$E(B - V)$	0.32	0.32 ± 0.04		0.34 ± 0.04	0.26 ± 0.04	0.08	0.31 ± 0.04	0.22 ± 0.04	0.09
$T_e[\text{O III}]$...	2.41 ± 0.25	...	1.44 ± 0.10	1.29 ± 0.10	0.15	2.28 ± 0.90	1.80 ± 0.10	0.48
O_{32}	11.4	14.1	2.7	7.1	7.7	0.6	30.1	17.3	12.8
$12 + \log(\text{O}/\text{H})$	7.54	7.12 ± 0.12	0.42	8.03 ± 0.12	8.17 ± 0.12	0.14	7.45 ± 0.07	7.73 ± 0.08	0.28
$\log(\text{C}/\text{O})$	-0.23	-0.83 ± 0.38	0.60
$\log(\text{Ne}/\text{O})$	-0.76	-0.52 ± 0.15	0.24	-0.64 ± 0.13	-0.64 ± 0.17	0.00	-0.58 ± 0.06	-0.58 ± 0.09	0.00

Note. For each galaxy, we list the properties from the first column for both the o007 and o008 visits, followed by the difference between each pair of measurements. The first row provides the redshifts measured in this work. The second through fourth rows list our calculated nebular properties for reddening, $E(B - V)$; electron temperature, T_e (10^4 K); and ionization, as represented by the [O III] $\lambda 5007$ /[O II] $\lambda 3727$ line ratio. The reddening values were calculated using the $H\delta/H\beta$ ratio and the Cardelli et al. (1989) reddening law. Electron temperatures were calculated from the [O III] $\lambda 4363/\lambda 5007$ line ratio and are given in units of 10^4 K. The fifth through seventh rows list the individual values and comparative differences for the derived abundances: $12 + \log(\text{O}/\text{H})$, $\log(\text{C}/\text{O})$, and $\log(\text{Ne}/\text{O})$.

^a In italic the spectrum affected by shutter closures (see Curti et al. 2023). Assuming $T_e = 16,000$ K to calculate the chemical abundances.

accounted for to produce consistent and reliable results. For our calculations, we have used the deblended flux measurement of [O III] $\lambda 4363$ to calculate $T_e([\text{O III}])$ for the o008 visit of s04590.

4.2. Total and Relative Abundances

4.2.1. $12 + \log(\text{O}/\text{H})$

The most common method of directly determining O/H abundances involves using $T_e[\text{O III}]$ measurements and reddening-corrected line fluxes to calculate their respective ionic abundances, summing these ionic abundances, and correcting for any significant unseen ionization states. In typical H II regions, O^+ and O^{+2} are the dominant ions and can be determined from the [O II] $\lambda 3727$ and [O III] $\lambda\lambda 4959, 5007$ emission lines. In fact, even in extreme emission line galaxies, which show strong detections of very high ionization emission lines (e.g., C IV $\lambda\lambda 1548, 1550$, He II $\lambda\lambda 1640, 4686$, [Fe V] $\lambda 4227$, [Ar IV] $\lambda\lambda 4711, 4740$), the O^0 and O^{+3} ions each compose $\lesssim 4\%$ of the total O ions and thus can be ignored. Therefore, we calculate O^{+2}/H^+ using the $T_e[\text{O III}]$ measurements and O^+/H^+ using the Garnett (1992) $T_e - T_e$ relations to estimate $T_e[\text{O II}]$ and add these ionic abundances together to determine the total O/H abundance. The resulting $12 + \log(\text{O}/\text{H})$ abundances are reported in Table 2. In general, the metallicities for the $z > 7$ galaxies are metal-poor ($12 + \log(\text{O}/\text{H}) < 8.2$ or $Z_{\text{neb.}} \lesssim 0.3 Z_{\odot}$). To explore the impact of the highly uncertain reddening correction, we also calculated the metallicity using uncorrected line fluxes ($E(B - V) = 0$), finding that the O/H abundances decrease by 0.12 dex, on average, which is within the uncertainties estimated in this study (see also Curti et al. 2023).

4.2.2. Ionization Parameter

Another key nebular property is the ionization parameter, $\log U$, which provides a measure of the strength of the ionizing radiation field. Here we use a common proxy for ionization parameter, O_{32} , defined by the [O III] $\lambda 5007/\lambda 3727$ ratio. The resulting O_{32} values for the present sample span a large range of high to very high ratios with $O_{32} \approx 7$ for s06335, $O_{32} \approx 17$ for s04590, and $O_{32} \approx 30$ for s10612. Such high values of O_{32} are often associated with extreme emission line galaxies and/or

LyC escape in the nearby universe (e.g., Izotov et al. 2016; Senchyna et al. 2017; Berg et al. 2021).

4.2.3. Relative C/O and Ne/O Abundances

The high redshift of the s04590 spectrum allows a measure of the C III] $\lambda\lambda 1907, 1909$ flux and, subsequently, the relative C^{+2} ionic abundance. Owing to the similar ionization and excitation energies of the C^{+2} and O^{+2} ions, relative C/O abundances are typically determined from the $\text{C}^{+2}/\text{O}^{+2}$ ratio. For high-ionization nebulae, such as the $z > 7$ galaxies investigated here, we must also consider carbon contributions from the C^{+3} species to avoid underestimating the true C/O abundance. To account for the potential contribution from C^{+3} , we use the photoionization model-derived C ionization correction factor (ICF) of Berg et al. (2019a), which is determined using the ionization parameter. In turn, we determine the ionization parameter based on the $\log([\text{O III}] \lambda 5007/[\text{O II}] \lambda 3727)$ ratio and the relationship provided by Berg et al. (2019a).

For Ne, we have used the high-ionization [Ne III] $\lambda 3869$ line to calculate the ionic abundances of $\text{Ne}^{+2}/\text{O}^{+2}$. To account for unseen ions of Ne, we use the ICF provided by Amayo et al. (2021). Similar to the method for C, this ICF is based on photoionization models and determined as a function of the ionization parameter ($[\text{O III}] \lambda 5007/[\text{O II}] \lambda 3727$). Amayo et al. (2021) provided relationships for the Ne ICF as a function of $\text{O}^{+2}/(\text{O}^+ + \text{O}^{+2})$ ratio to characterize the average ionization within the nebula. We list the resulting Ne/O abundances for each galaxy and the C/O abundance for J04590 in Table 2.

5. Discussion

5.1. The MZR

The relationship between stellar mass and gas-phase metallicity (the MZR) provides a critical probe of galaxy evolution. The MZR is shaped by the cumulative galaxy evolutionary processes, where star formation builds up metals through nucleosynthesis, while enriched outflows remove metals and pristine gas inflows dilute the metals in the ISM (e.g., Tremonti et al. 2004; Dalcanton 2007; Peeples & Shankar 2011; Zahid et al. 2014). Because accurate MZR trends require direct abundance measurements, the evolution of the MZR has only been investigated at moderate redshifts (e.g.,

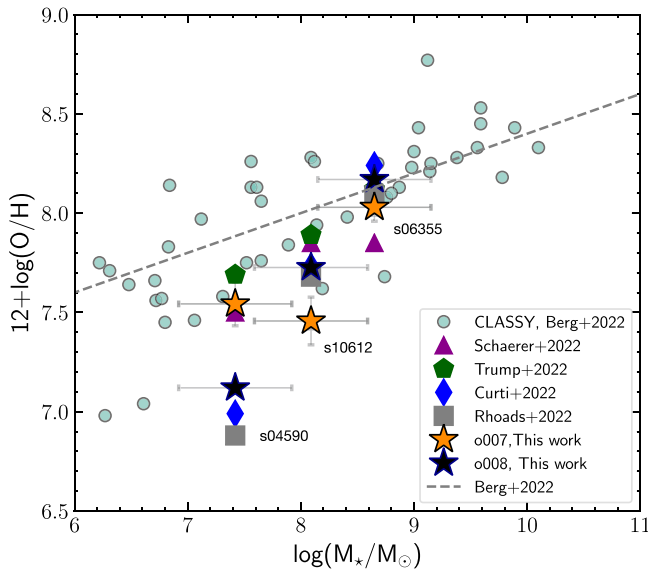


Figure 2. Stellar mass vs. gas-phase metallicity ($12 + \log(\text{O}/\text{H})$) relationship for star-forming galaxies. The $z > 7$ galaxies are plotted as stars with stellar masses derived by Carnall et al. (2023). Additional recent metallicity determinations are labeled from Schaerer et al. (2022; triangles), Trump et al. (2022; pentagons), Curti et al. (2023; diamonds), and Rhoads et al. (2022; squares). For the purpose of comparing to local galaxy populations, we plot the UV-bright CLASSY sample (circles and dashed line; Berg et al. 2022).

Sanders et al. 2021) and typically only probes the most massive systems. The advent of JWST opens a window onto the distant universe that pushes the MZR to higher redshifts and lower masses than ever before.

In Figure 2, we use our O/H abundance determinations with the stellar masses reported by Carnall et al. (2023) to plot the MZR for the three $z > 7$ galaxies of JWST/NIRSpec. Following Trump et al. (2022), we adopt large (0.5 dex) error bars to account for the systematic offset of the Carnall et al. (2023) masses from the Schaerer et al. (2022) and Curti et al. (2023) masses. Figure 2 compares other recent analyses of these galaxies from Schaerer et al. (2022), Trump et al. (2022), Curti et al. (2023), and Rhoads et al. (2022). Note that the results of Schaerer et al. (2022) and Rhoads et al. (2022) are obtained using the original JWST Science Calibration Pipeline spectra, while Trump et al. (2022) and Curti et al. (2023) used their own postprocessing reduction. All four studies determined abundances from the combined o007 and o008 spectra for each galaxy.⁹ Additionally, each of these studies used different methods to calculate metallicity (see, e.g., Trump et al. 2022). In general, we find that our O/H measurements for s06335 and s10612 are consistent with the literature determinations, with an overall dispersion of $\sigma \sim 0.5$ dex. On the other hand, the abundances for s04590 are separated into two distinct clumps in Figure 2, which could be due to the odd line profile between the two different visits, indicating the sensitivity of the T_e determination to uncertainties in the [O III] $\lambda 4363$ flux (Arellano-Córdova et al. 2016). However, a definitive interpretation is complicated due to the differences in reduction and calculation methods.

To investigate the evolution of the MZR with redshift, Figure 2 compares the $z > 7$ galaxies to the $z \sim 0$ MZR trends from the COS Legacy Archive Spectroscopic SurveY

(CLASSY; Berg et al. 2022). While for s06355 and s10612, the values of metallicity are nearly consistent with previous determinations within the uncertainties, the results for s04590 show significant differences, which are divided into two different ranges of metallicity (see Figure 2). In particular, if the higher abundance of s04590 is adopted, the slope of $z > 7$ is consistent with the $z \sim 0$ trend, suggesting little redshift evolution. This would suggest that the physical properties that set the MZR at $z \sim 0$ (outflows of metal-enriched gas and inflows of pristine gas) are already in place by $z \sim 7$, and their relative strengths do not significantly evolve with time. Alternatively, if we adopt the lower s04590 abundance, the $z > 7$ MZR has a much steeper slope. The slope of the MZR is largely shaped by the level of feedback in galaxies, where a steeper slope would imply (1) an increased importance of inflows of pristine gas at lower masses/metallicities and/or (2) weaker outflows of enriched gas, allowing the O/H abundances to more quickly build up with stellar mass than seen at $z \sim 0$. Although the analysis based on the result of s04590 might suggest a change in the slope of the MZR at $z > 7$, its position in the MZR is still consistent with the observed values at $z \sim 0$ due to the dispersion observed in $z \sim 0$ galaxies (Berg et al. 2022; $\sigma = 0.29$ dex). Then, the interpretation of the MZR at $z > 7$ strongly depends on the data quality/reductions and the sample size. Therefore, large samples of $z > 7$ galaxies with high S/N and robust absolute flux calibration are needed to further constrain the evolution of the MZR.

5.2. Ionization Parameter Evolution

Table 2 lists the O_{32} values measured from the o007 and o008 visits for each galaxy. The ionization of the $z > 7$ sample is high, on average: $\langle \text{O}_{32} \rangle = 15$, which is consistent with studies of nearby extreme emission line galaxies that are typical of LyC escape (Izotov et al. 2012, 2016; Senchyna et al. 2019) but much higher than the general $z \sim 0$ galaxy population. In comparison to the recent literature, we find that the O_{32} value of o007 for s10612 is consistent with the result provided by Curti et al. (2023; $\text{O}_{32} = 27.3$), but the o008 visit has a much lower value of $\text{O}_{32} = 17.3$. Additionally, our O_{32} values are much higher in general than those reported by Schaerer et al. (2022), especially for s04590 and s10612. The differences in reported O_{32} values are likely due to the issues with the current pipeline-produced 1D spectra (v1.6.1) and the inferred dust correction. This suggests that the O_{32} value strongly depends on the adopted reduction routine (e.g., the narrow extraction aperture) and may dramatically change as the NIRSpec reference files and reduction routines are refined.

5.3. The C/O–O/H and Ne/O–O/H Trends

We present the C/O versus O/H relationship for our $z > 7$ sample in the top left panel of Figure 3. Unfortunately, only s04590 has a high enough redshift to measure the FUV C III] $\lambda\lambda 1907, 1909$ lines; thus, we only have C/O results for this galaxy. In comparison, we include the $z \sim 0$ and 2 trends from Berg et al. (2019b). For $12 + \log(\text{O}/\text{H}) \lesssim 8.0$, these trends derive C/O using the rest-frame FUV O III] $\lambda 1666$ and C III] $\lambda\lambda 1907, 1909$ collisionally excited lines, while the C/O abundance at higher metallicities is derived using the rest-frame optical C II $\lambda 4267$ recombination line. This first look and analysis of the $\log(\text{C}/\text{O})$ abundance at $z > 7$ (from the o008 visit) shows a value of $\log(\text{C}/\text{O})$ lower than the average

⁹ Note that Curti et al. (2023) took care to remove a nod of the o007 visit for s04590 that was affected by a failed shutter.

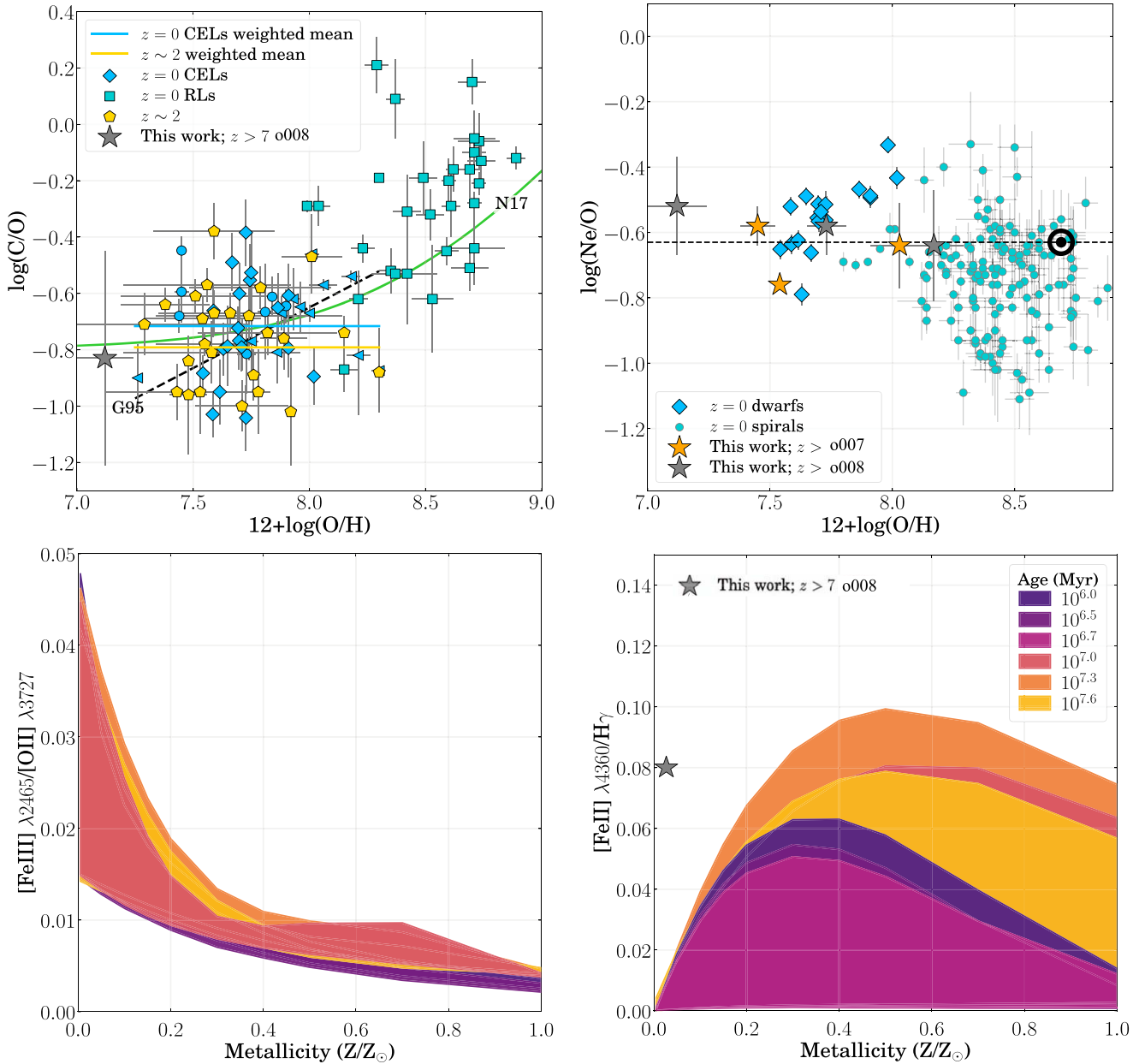


Figure 3. Top left: C/O vs. O/H relationship taken from Berg et al. (2019b) for $z \sim 0$ and 2 galaxies. The dashed and solid lines represent the relationships of Garnett et al. (1995) and Nicholls et al. (2017). The results for s04590 are shown as a gray star for the o008 visit. Top right: Ne/O vs. O/H relationship for $z \sim 0$ low-metallicity dwarf galaxies and H II regions of spiral galaxies. The Ne/O ratios for the $z > 7$ NIRSpc galaxies are displayed as gray and cyan symbols. The black dashed line indicates the solar Ne/O value (-0.63 ± 0.05 ; Asplund et al. 2021). Bottom row: Photoionization models of the [Fe III] $\lambda_{2465}/[O II] \lambda_{3727}$ flux (left) and [Fe II] $\lambda_{4360}/H\gamma$ flux (right) vs. metallicity. The value derived for the Fe III] $\lambda_{2465}/[O II] \lambda_{3727}$ ratio is outside the range of the models (bottom left panel).

observed for $z \sim 0$ and 2 galaxies. However, the $\log(C/O)$ values for $z \sim 0-2$ galaxies show a large dispersion at low metallicity, $\sigma \sim 0.17$ dex (Berg et al. 2019b). Therefore, the $\log(C/O)$ value derived for s4590 remains consistent with the observed values in local star-forming galaxies. Interestingly, from modeling the chemical evolution of C/O of metal-poor galaxies, Berg et al. (2019b) found that the C/O ratio is very sensitive to both the detailed star formation history and supernova feedback. Along these lines, the $z > 7$ C/O abundance plotted in Figure 3 points to either lower star formation efficiencies, a longer burst duration, a larger effective oxygen yield (little ejection of oxygen in outflows), or some combination of these. However, note that the C/O ratio for

s04590 (see Table 2) is highly uncertain, and robust measurements are required to determine what drives the chemical abundances at $z > 7$. In Table 2, we also provide the C/O ratio derived from the o007 spectrum. Such a value is significantly higher than the o008 visit and inconsistent with the $z \sim 0$ and 2 trends. A large C/O value would be our first hint that the C/O–O/H relationship evolves significantly over cosmic time, where pristine inflows were larger and/or effective oxygen yields were lower at $z > 7$. However, the detection of C III] $\lambda\lambda 1907, 1909$ lines in the o007 visit is uncertain, and the C/O ratio depends on our assumption of $T_e = 16,000$ K.

In the top right panel of Figure 3, we show the relation between $\log(\text{Ne}/\text{O})$ and metallicity for our $z > 7$ sample. For a local comparison, we also plot a sample of dwarf galaxies (Berg et al. 2019b) and H II regions from spiral galaxies (Berg et al. 2020). In principle, Ne is an α -element and thus expected to be constant with O/H because massive stars produce both elements on the same timescales (see, e.g., Arellano-Córdova et al. 2020; Rogers et al. 2021). For our $z > 7$ sample, we find consistent Ne/O abundances with the $z \sim 0$ low-metallicity dwarf galaxies. Despite the large observational uncertainties associated with this study (e.g., absolute flux calibration and possible artifacts in relevant emission lines), all of the individual Ne/O measurements are consistent within 0.2 dex of a solar abundance (Asplund et al. 2021).

In addition, to investigate the impact of the reddening in determining the Ne/O ratio, we derived the Ne/O abundance ratio using the intensities of [O II], [O III], and [Ne III] and $T_e[\text{O III}]$ reported in Curti et al. (2023). The intensities were corrected by reddening using the A_v values also reported in Curti et al. (2023). We calculated values of the Ne/O ratios of -0.71 ± 0.25 , -0.67 ± 0.12 , and -0.58 ± 0.17 for s04590, s06355, and s10612. Such results are consistent with respect to those derived in this work (see Table 2). However, for the o008 visit of s04590, we reported a value 0.19 dex higher than that obtained using the measurements of Curti et al. (2023) but consistent within the errors. Despite the different approaches used to derive reddening and $T_e[\text{O III}]$, both results are in agreement with the Ne/O abundance ratios estimated in local star-forming regions at low metallicity ($12 + \log(\text{O}/\text{H}) < 8.0$) and with respect to the solar abundance as reported in local star-forming regions (see, e.g., Dors et al. 2013).

Therefore, we find that Ne/O abundances can be robustly determined from JWST observations of high-redshift galaxies, and at least in this analysis, there is no evidence for cosmic evolution of the Ne/O–O/H trend. We stress that this first look at the C and Ne lines and their respective ionic abundances and the Ne/O and C/O ratios provide a first reference of the expected values at $z > 7$ compared to local galaxies and the challenges in deriving robust measurements of other metals in addition to O/H.

5.4. Fe/O Abundance at High Redshift

While collisionally excited emission lines are commonly observed for one or two species of Fe in $z = 0$ H II regions, Fe abundance determinations are often avoided due to the importance of dust depletion, accurate ICFs, and fluorescence (Rodríguez 1999, 2002). However, several recent studies have revived the interest in Fe abundances by suggesting that enhanced α/Fe abundance ratios are responsible for the extremely hard radiation fields inferred from the stellar continua and emission line ratios in chemically young $z \sim 2$ galaxies (e.g., Steidel et al. 2018; Shapley et al. 2019; Topping et al. 2020). Given the importance of α/Fe (e.g., O/Fe) abundances to interpret the ionizing continua of early galaxies, we were motivated to investigate the Fe/O abundance in the $z > 7$ galaxies.

Perhaps unsurprisingly for chemically young $z > 7$ galaxies, we do not detect any significant Fe emission lines in the s06355 and s1016 spectra. The s04590 spectrum, on the other hand, shows tentative evidence of Fe emission via the [Fe II] $\lambda\lambda 4287$, 4360 and [Fe III] $\lambda\lambda 2465$, 5271 lines. While robust Fe/O abundances cannot be produced from these lines alone (see

discussion in Berg et al. 2021), we can gain some insight by examining the [Fe III]/[O II] line ratio, whose ions have similar ionization potentials. In the bottom panels of Figure 3, we plot the photoionization grid of Berg et al. (2019b) of [Fe III] $\lambda 2465$ /[O II] $\lambda 3727$ versus metallicity (left) and [Fe II] $\lambda 4360$ /H γ (right). The BPASS single-burst models with ages of [$10^{6.0}$, $10^{6.5}$, $10^{6.7}$, $10^{7.0}$, $10^{7.3}$, $10^{7.6}$] yr were used as the input ionizing spectrum, as indicated by the different-colored shaded regions. The vertical shading represents the maximum range of values produced considering a range of ionization parameters from $\log U = -1$ to -4 . We overplot the line ratios measured for the o008 visit of s04590; however, the model ratios fail to reach the tentative detections of the line ratios for both the [Fe III]/[O II] and [Fe II]/H γ ratios. In particular, for [Fe III]/[O II], we obtain a high value of such a ratio, which could be due to the high uncertainty in the detection of [Fe III] in the o008 visit. However, this mismatch may indicate that Fe/O abundances are higher at $z > 7$ than $z \sim 0$ (in contrast to the enhanced α -Fe theory), which could result if high-redshift galaxies have a low effective yield of oxygen, as suggested by the enhanced C/O abundance of the o007 visit of s04590. At the same time, the current Fe detection is very tentative and may be overestimated due to the low S/N < 3 , especially given the lack of a secure flux calibration. Therefore, the Fe/O will need to be revisited.

6. Conclusions

We analyze the rest-frame near-UV and optical spectra of three $z > 7$ galaxies observed with Early Release Observations from NIRSpec on JWST. Each of the three galaxies (source IDs s04590, s06355, and s10612) were observed for two visits (o007 and o008), allowing us to assess the quality of the spectra by examining the consistency of the emission features. However, the default spectra from the JWST Science Calibration Pipeline (v1.6.1) are not yet fully calibrated; thus, the exact reduction process changes the delivered spectrum. Of particular importance is the lack of a robust relative flux calibration, the effects of failed shutter openings, and the potential wavelength-dependent light loss during 1D extraction apertures (see a complete discussion in Trump et al. 2022). To mitigate some of these effects, our analysis used the postprocessed JWST/NIRSpec spectra from Trump et al. (2022) and P. Arrabal Haro et al. 2022, in preparation, which includes a custom aperture extraction and flux calibration. The resulting spectra still have large uncertainties, so we take extra caution to use nearby (when possible) emission line ratios to calculate the physical conditions, chemical abundances, and ionization parameters for the $z > 7$ galaxies. Further, the o007 spectrum of s04590 is likely affected by a shutter failure, causing a large discrepancy in its derived properties relative to the o008 spectrum.

With these data reduction caveats in mind, our main results are summarized as follows.

1. The temperature-sensitive [O III] $\lambda 4363$ line is detected in the two different visits (o007 and o008) of each high- z galaxy, allowing the computation of $T_e[\text{O III}]$ for 5/6 of the individual spectra. However, we confirm the nonphysical result of $T_e[\text{O III}]$ derived for the o007 visit of s04590 (the visit with the failed shutter) reported by Curti et al. (2023). Based on the broad, asymmetric emission line profile of the [O III] $\lambda 4363$ feature in the

o008 visit of s04590, we explore a possible reason for this result, indicating a potential contamination of the line by either the [Fe II] λ 4360 line or a spectral artifact.

2. Using our $T_e[\text{O III}]$ values, we derived direct-method O/H abundances for the $z > 7$ galaxies. Recent studies from Schaerer et al. (2022), Trump et al. (2022), Curti et al. (2023), and Rhoads et al. (2022) have also reported metallicity measurements, but all use spectra from combined visits and a variety of analysis methods. We find our measurements for s06335 and s10612 to be consistent within 2σ between o007 and o008 and with those recently published in the literature. For s04590, however, we find our two measurements to be discrepant by 0.42 dex, where the o007 measurement (the visit with the failed shutter) is consistent with the studies of Trump et al. (2022) and Schaerer et al. (2022), and o008 is well aligned with the values found by Curti et al. (2023) and Rhoads et al. (2022). We use our O/H results to investigate the mass–metallicity relationship (MZR), finding that the s04590 measurement changes the $z > 7$ trend and that its large uncertainty significantly impacts our interpretation of the MZR. (1) If the o007 (higher) abundance is adopted for s04590 (the visit with the failed shutter), the $z > 7$ MZR is consistent with the $z > 0$ trend. (2) If the o008 (lower) abundance is adopted, the slope of the $z > 7$ MZR becomes much steeper than the $z > 0$ MZR, suggesting that different physical processes drive the shape of the MZR at $z > 7$ that allow the O/H abundance to build up more quickly. However, due to the significant variation of the metallicity in s04590 derived in both visits and other studies from the literature, a detailed physical interpretation of the MZR cannot be done until larger samples of higher-quality data are properly calibrated.
3. At the redshift of s04590 ($z = 8.495$), the NIRSpec spectrum covers the C III] $\lambda\lambda$ 1907, 1909 lines. We measured this feature and used it to estimate the relative C/O abundance for s04590, the most distant C/O measurement to date. When compared to $z \sim 0$ – 2 low-metallicity dwarf galaxies, the o008 measurement is consistent given the large dispersion of the log C/O values of $z \sim 0$ – 2 galaxies; therefore, there is no evidence of an evolution in the C/O versus O/H relationship.
4. We measured the first Ne/O abundance for $z > 7$ galaxies using the isolated [Ne III] λ 3868 emission line, which is detected in all three galaxies. Our Ne/O abundances are consistent with a constant trend with O/H, as expected for α -element abundance ratios. Our results are also in agreement with $z \sim 0$ low-metallicity galaxies, indicating that there is no redshift evolution of the Ne/O abundance.
5. We analyzed the tentative detection of [Fe II] λ 4360 and [Fe III] λ 2465 in s04590. However, these flux measurements should be taken with caution. We find that an [Fe III]/[O II] ratio is large compared to $z \sim 0$ photoionization models, probably due the high uncertainty in the measurement of [Fe III] λ 2465. On the other hand, our simultaneous fit of the potentially blended [Fe II] λ 4360 + [O III] λ 4363 lines yields an [Fe II] λ 4360/ $H\gamma$ ratio that is only reproduced by the photoionization models at higher metallicities. This may indicate significant Fe enrichment relative to O. We postulate that massive outflows of O-enriched gas at very early cosmic times













could decrease the O abundance relative to Fe to produce these large flux ratios. However, the tentative detection of Fe lines in s04590 should be revised, and upcoming JWST data with robust flux calibration and high-S/N observation will allow us to assess the detection of such lines at $z > 7$ galaxies.

In summary, JWST/NIRSpec spectra of high-redshift galaxies are opening an important window onto the evolution of the first galaxies, such as this first look at the abundance patterns of $z > 7$ galaxies. Thus, significant advancements in this area are imminent, but a robust interpretation will require larger samples of high-redshift galaxy observations, higher-S/N spectra, and further refinement of the spectral reduction.

We thank the referee for thoughtful feedback that improved this letter. The Early Release Observations and associated materials were developed, executed, and compiled by the ERO production team: Hannah Braun, Claire Blome, Matthew Brown, Margaret Carruthers, Dan Coe, Joseph DePasquale, Nestor Espinoza, Macarena Garcia Marin, Karl Gordon, Alaina Henry, Leah Hustak, Andi James, Ann Jenkins, Anton Koekemoer, Stephanie LaMassa, David Law, Alexandra Lockwood, Amaya Moro-Martin, Susan Mullally, Alyssa Pagan, Dani Player, Klaus Pontoppidan, Charles Proffitt, Christine Pulliam, Leah Ramsay, Swara Ravindranath, Neill Reid, Massimo Robberto, Elena Sabbi, and Leonardo Ubeda. The EROs were also made possible by the foundational efforts and support from the JWST instruments, STScI planning and scheduling, and data management teams.

The CEERS team thanks Pierre Ferruit and the NIRSpec GTO team for providing NIRSpec IPS simulated data and general good counsel and the STScI NIRSpec instrument team for extensive assistance regarding the JWST Pipeline and data simulations.

ORCID iDs

- Karla Z. Arellano-Córdova  <https://orcid.org/0000-0002-2644-3518>
 Danielle A. Berg  <https://orcid.org/0000-0002-4153-053X>
 John Chisholm  <https://orcid.org/0000-0002-0302-2577>
 Pablo Arrabal Haro  <https://orcid.org/0000-0002-7959-8783>
 Mark Dickinson  <https://orcid.org/0000-0001-5414-5131>
 Steven L. Finkelstein  <https://orcid.org/0000-0001-8519-1130>
 Floriane Leclercq  <https://orcid.org/0000-0002-6085-5073>
 Noah S. J. Rogers  <https://orcid.org/0000-0002-0361-8223>
 Raymond C. Simons  <https://orcid.org/0000-0002-6386-7299>
 Evan D. Skillman  <https://orcid.org/0000-0003-0605-8732>
 Jonathan R. Trump  <https://orcid.org/0000-0002-1410-0470>
 Jeyhan S. Kartaltepe  <https://orcid.org/0000-0001-9187-3605>

References

- Amayo, A., Delgado-Inglada, G., & Stasińska, G. 2021, *MNRAS*, 505, 2361
 Arellano-Córdova, K. Z., Esteban, C., García-Rojas, J., & Méndez-Delgado, J. E. 2020, *MNRAS*, 496, 1051
 Arellano-Córdova, K. Z., Mingozzi, M., Berg, D. A., et al. 2022, *ApJ*, 935, 74
 Arellano-Córdova, K. Z., & Rodríguez, M. 2020, *MNRAS*, 497, 672
 Arellano-Córdova, K. Z., Rodríguez, M., Mayya, Y. D., & Rosa-González, D. 2016, *MNRAS*, 455, 2627
 Asplund, M., Amarsi, A. M., & Grevesse, N. 2021, *A&A*, 653, A141
 Berg, D. A., Chisholm, J., Erb, D. K., et al. 2019a, *ApJL*, 878, L3

- Berg, D. A., Chisholm, J., Erb, D. K., et al. 2021, *ApJ*, **922**, 170
- Berg, D. A., Erb, D. K., Henry, R. B. C., Skillman, E. D., & McQuinn, K. B. W. 2019b, *ApJ*, **874**, 93
- Berg, D. A., James, B. L., King, T., et al. 2022, *ApJS*, **261**, 31
- Berg, D. A., Pogge, R. W., Skillman, E. D., et al. 2020, *ApJ*, **893**, 96
- Berg, D. A., Skillman, E. D., Garnett, D. R., et al. 2013, *ApJ*, **775**, 128
- Brinchmann, J. 2022, arXiv:2208.07467
- Cardelli, J. A., Clayton, G. C., & Mathis, J. S. 1989, *ApJ*, **345**, 245
- Carnall, A. C., Begley, R., McLeod, D. J., et al. 2023, *MNRAS*, **518**, L45
- Chisholm, J., Saldana-Lopez, A., Flury, S., et al. 2022, *MNRAS*, **517**, 5104
- Curti, M., Cresci, G., Mannucci, F., et al. 2017, *MNRAS*, **465**, 1384
- Curti, M., D'Eugenio, F., Carniani, S., et al. 2023, *MNRAS*, **518**, 425
- Dalcanton, J. J. 2007, *ApJ*, **658**, 941
- Dors, O. L., Hägele, G. F., Cardaci, M. V., et al. 2013, *MNRAS*, **432**, 2512
- Draine, B. T. 2011, *Physics of the Interstellar and Intergalactic Medium* (Princeton, NJ: Princeton Univ. Press)
- Ebeling, H., Jones, L. R., Fairley, B. W., et al. 2001, *ApJL*, **548**, L23
- Ferruit, P., Jakobsen, P., Giardino, G., et al. 2022, *A&A*, **661**, A81
- Finkelstein, S. L., Bagley, M. B., Arrabal Haro, P., et al. 2022, *ApJL*, in press, arXiv:2207.12474
- Finkelstein, S. L., D'Aloisio, A., Paardekooper, J.-P., et al. 2019, *ApJ*, **879**, 36
- Fontanot, F., Cristiani, S., Pfrommer, C., Cupani, G., & Vanzella, E. 2014, *MNRAS*, **438**, 2097
- Garnett, D. R. 1992, *AJ*, **103**, 1330
- Garnett, D. R., Skillman, E. D., Dufour, R. J., et al. 1995, *ApJ*, **443**, 64
- Henry, R. B. C., Edmunds, M. G., & Köppen, J. 2000, *ApJ*, **541**, 660
- Hutchison, T. A., Papovich, C., Finkelstein, S. L., et al. 2019, *ApJ*, **879**, 70
- Izotov, Y. I., Schaerer, D., Thuan, T. X., et al. 2016, *MNRAS*, **461**, 3683
- Izotov, Y. I., Thuan, T. X., & Guseva, N. G. 2012, *A&A*, **546**, A122
- Jakobsen, P., Ferruit, P., Alves de Oliveira, C., et al. 2022, *A&A*, **661**, A80
- Kewley, L. J., Nicholls, D. C., & Sutherland, R. S. 2019, *ARA&A*, **57**, 511
- Lagache, G., Cousin, M., & Chatzikos, M. 2018, *A&A*, **609**, A130
- Li, Q., Narayanan, D., & Davé, R. 2019, *MNRAS*, **490**, 1425
- Luridiana, V., Morisset, C., & Shaw, R. A. 2015, *A&A*, **573**, A42
- Madau, P., & Haardt, F. 2015, *ApJL*, **813**, L8
- Maiolino, R., & Mannucci, F. 2019, *A&ARv*, **27**, 3
- Méndez-Delgado, J. E., Henney, W. J., Esteban, C., et al. 2021, *ApJ*, **918**, 27
- Naidu, R. P., Tacchella, S., Mason, C. A., et al. 2020, *ApJ*, **892**, 109
- Nicholls, D. C., Sutherland, R. S., Dopita, M. A., Kewley, L. J., & Groves, B. A. 2017, *MNRAS*, **466**, 4403
- Peeples, M. S., & Shankar, F. 2011, *MNRAS*, **417**, 2962
- Piqueras, L., Legros, E., Pons, A., et al. 2010, *Proc. SPIE*, **7738**, 773812
- Pontoppidan, K., Barrientes, J., Blome, C., et al. 2022, *ApJL*, **936**, L14
- Reddy, N. A., Steidel, C. C., Pettini, M., Bogosavljević, M., & Shapley, A. E. 2016, *ApJ*, **828**, 108
- Repp, A., & Ebeling, H. 2018, *MNRAS*, **479**, 844
- Rhoads, J. E., Wold, I. G. B., Harish, S., et al. 2022, arXiv:2207.13020
- Rodríguez, M. 1999, *A&A*, **348**, 222
- Rodríguez, M. 2002, *A&A*, **389**, 556
- Rogers, N. S. J., Skillman, E. D., Pogge, R. W., et al. 2021, *ApJ*, **915**, 21
- Rogers, N. S. J., Skillman, E. D., Pogge, R. W., et al. 2022, *ApJ*, **939**, 44
- Saldana-Lopez, A., Schaerer, D., Chisholm, J., et al. 2022, *A&A*, **663**, A59
- Sanders, R. L., Shapley, A. E., Jones, T., et al. 2021, *ApJ*, **914**, 19
- Schaerer, D., Marques-Chaves, R., Barrufet, L., et al. 2022, *A&A*, **665**, L4
- Senchyna, P., Stark, D. P., Chevallard, J., et al. 2019, *MNRAS*, **488**, 3492
- Senchyna, P., Stark, D. P., Vidal-García, A., et al. 2017, *MNRAS*, **472**, 2608
- Shapley, A. E., Cullen, F., Dunlop, J. S., et al. 2020, *ApJL*, **903**, L16
- Shapley, A. E., Sanders, R. L., Shao, P., et al. 2019, *ApJL*, **881**, L35
- Stark, D. P. 2016, *ARA&A*, **54**, 761
- Steidel, C. C., Bogosavljević, M., Shapley, A. E., et al. 2018, *ApJ*, **869**, 123
- Steidel, C. C., Strom, A. L., Pettini, M., et al. 2016, *ApJ*, **826**, 159
- Tinsley, B. M. 1980, *FCPh*, **5**, 287
- Topping, M. W., Shapley, A. E., Reddy, N. A., et al. 2020, *MNRAS*, **495**, 4430
- Tremonti, C. A., Heckman, T. M., Kauffmann, G., et al. 2004, *ApJ*, **613**, 898
- Trump, J. R., Arrabal Haro, P., et al. 2022, arXiv:2207.12388
- Wise, J. H., Demchenko, V. G., Halicek, M. T., et al. 2014, *MNRAS*, **442**, 2560
- Zahid, H. J., Dima, G. I., Kudritzki, R.-P., et al. 2014, *ApJ*, **791**, 130